Journal of Solid State Chemistry **147,** 647–656 (1999)
Article ID jssc.1999.8438, available online at http://www.idealibrary.com on IDEAL®

# Structural Transformations in the Fluorinated T* Phase

J. Hadermann,* A. M. Abakumov,*,† O. I. Lebedev,* G. Van Tendeloo,* M. G. Rozova,† R. V. Shpanchenko,† B. Ph. Pavljuk,† E. M. Kopnin,† and E. V. Antipov†

*EMAT, University of Antwerp (RUCA), Groenenborgerlaan 171, B-2020 Antwerp, Belgium; and †Department of Chemistry, Moscow State University, 119899 Moscow, Russia

Received March 12, 1999; in revised form June 9, 1999; accepted June 29, 1999

**$LaHo_{0.75}Sr_{0.25}CuO_{3.9}$, representing the intergrowth of rock salt, fluorite-type slabs, and ($CuO_2$)-layers have been fluorinated using $XeF_2$ as a soft fluorinating agent at temperatures ranging from 200 to 400°C. The resulting structures were studied by a combination of X-ray diffraction, electron diffraction, and high resolution electron microscopy. The samples show a complex microstructure with alternating bands of two fluorinated phases with different structures. Narrow bands (60–100 Å) of a monoclinic phase ($a_m = a\sqrt{2} \approx 5.5$ Å, $b_m = a\sqrt{2} \approx 5.5$ Å, $c_m = c = 12.84$ Å, $\beta = 91.4°$) are formed in an orthorhombic matrix. The formation of the monoclinic superstructure (*A* phase) is accompanied by an equal anion arrangement within the initially different rock salt and fluorite-type slabs and by cooperative displacements of the *A* cations. In the structure of the less fluorinated *B* phase, the fluorite slabs are not affected by fluorination. Fluorine atoms occupy part of the interstitial positions in the rock salt slabs with partial removal of apical oxygen atoms; this lies most probably at the origin of the incommensurate modulation of the *B* phase.** © 1999 Academic Press

*Key Words:* **fluorination; T*-phase; $LaHo_{0.75}Sr_{0.25}CuO_{3.9-x}F_y$.**

## INTRODUCTION

The rare-earth cuprates $Ln_2CuO_4$ can be converted into superconductors by a variation of the charge carrier concentration. It can be achieved either by a heterovalent cation replacement or by a change in the anion composition. The fluorination of $Ln_2CuO_4$ phases allows the induction of superconductivity in both types of rare-earth cuprates: T phase ($La_2CuO_4$-type structure) and T′ phase ($Nd_2CuO_4$-type structure). However, the origin of the appearance of superconductivity and the structural features of the fluorine accommodation are significantly different for the T and T′ phases. The partial replacement of oxygen by fluorine in the fluorite-like $Nd_2O_2$ slab of the $Nd_2CuO_4$ structure provides an increase of the electron concentration and the appearance of *n*-type superconductivity in $Nd_2CuO_{4-x}F_x$ (1–3). In contrast to this, the insertion of extra fluorine atoms is required for $La_2CuO_4$ to introduce holes in the conducting band. A superconducting phase with $T_c = 35$–$40$ K was obtained at small doping level (up to $La_2Cu(O,F)_{4.18}$) (4). The fluorination results in an increase of the orthorhombic distortion, but the structure of $La_2CuO_4$ remains almost unchanged (5). The additional anions are located in the interstices of the rock-salt-like $La_2O_2$ blocks (6).

An increase of the amount of inserted fluorine is usually connected with increasing the temperature of the treatment by the fluorinating agent. At temperatures of 230–250°C the orthorhombic $La_2CuO_4$ is transformed into a tetragonal $K_2NiF_4$-type structure. The anion exchange becomes the predominant reaction when the fluorination temperature increases above 300°C. The fluorine atoms occupy interstitial positions with the removal of neighboring apical oxygen, resulting in the transformation of part of the $CuO_6$ octahedra into $CuO_5$ pyramids. Blocks with occupied interstitial positions and removed apical oxygen atoms (fluorite slabs) alternate with the blocks of rock salt slabs in an ordered manner leading to a new monoclinic phase with ideal composition $La_2CuO_{3.6}F_{0.8}$ (7).

Another rare-earth cuprate with a structure closely related to those of the T and T′ phases is ($Ln$, $R$, $M$)$_2CuO_4$ ($R$, rare-earth cation smaller than $Ln$; $M$, Ba, Sr) known as the T* phase. Large $Ln$ together with $M$ and smaller $R$ cations are placed in an ordered manner forming rock-salt-like and fluorite-like slabs, respectively, which alternate with ($CuO_2$) layers along the *c*-axis of the tetragonal unit cell. The copper atoms have a fivefold square-pyramidal coordination (8) (Fig. 1). The neutron powder refinement of the fluorinated $La_{1.25}Dy_{0.75}CuO_{3.75}F_{0.5}$ compound revealed a transformation of the tetragonal structure into an orthorhombic one with cell parameters $a_o \approx b_o = \sqrt{2}a_t$, $c_o \approx c_t$ (9). The extra anions were found at the interstitial positions of the $La_2O_2$ rock salt block while no extra anions were found in the $Dy_{1.5}La_{0.5}O_2$ fluorite-type slab. However, the reasons for the orthorhombic distortion are still not clear. The goal of the present work is a structural study of the $LaHo_{0.75}Sr_{0.25}CuO_{3.9}$ T* phase fluorinated by $XeF_2$ at different treatment conditions.



0022-4596/99 $30.00

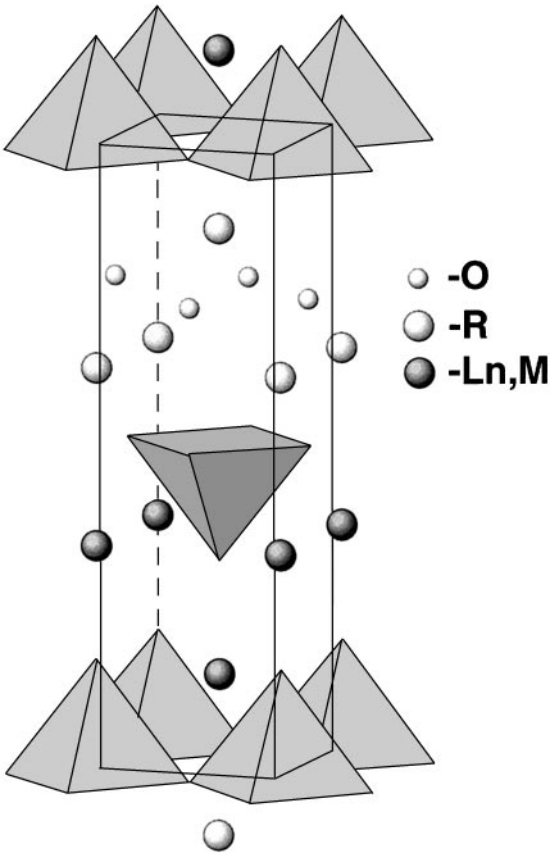


**FIG. 1.** The crystal structure of the T* phase. The $CuO_5$ pyramids are shown, *Ln* and *R* cations are shown as spheres with different darkness.

## EXPERIMENTAL

The $LaHo_{0.75}Sr_{0.25}CuO_{3.9}$ sample was prepared by a routine ceramic technique using $La_2O_3$, $Ho_2O_3$, $SrCO_3$, and CuO as initial reagents. Stoichiometric amounts of the compounds were intimately mixed, pressed into pellets, and heated in air at 1050°C for 40 h. The oxygen content was determined by iodometric titration. The obtained monophase $LaHo_{0.75}Sr_{0.25}CuO_{3.9}$ has lattice constants $a = 3.8368(4)$ Å, $c = 12.533(2)$ Å (space group $P4/nmm$), which are in good agreement with those previously published (10).

All operations with $XeF_2$ were carried out in a glove box filled with dried $N_2$. Then 0.4 g of the T* phase was mixed with $XeF_2$ (provided by the Laboratory of Inorganic Synthesis of the Institute of Applied Chemical Physics, Kurchatovskii Institute, Moscow, Russia) in a molar ratio of 1 : 1–1.5 and ground in an agate mortar. The mixture was placed in a Ni crucible and then into sealed copper tube. The samples were annealed at temperatures ranging from 200 to 400°C for 30–200 h and furnace cooled to room temperature.

The phase composition of the samples and the lattice parameters of the compounds were studied by X-ray diffraction using a focusing Guinier camera FR-552 ($CuK\alpha_1$ radiation, Ge internal standard).

AC susceptibility measurements were performed in the temperature range of 12–100 K at an external field amplitude of 1 Oe and a frequency of 27 Hz.

Electron diffraction (ED) and high resolution electron microscopy (HREM) were performed using a JEOL 4000EX instrument. EDX analysis and electron diffraction were performed using a Philips CM20 microscope with a LINK-2000 attachment. Image simulations were made using MacTempas software.

## RESULTS

The fluorination conditions of the different samples are listed in Table 1. The X-ray diffraction patterns of samples 2–5 can be interpreted as a superposition of two patterns of phases having the tetragonal T* structure but different cell parameters. The cell dimensions of the main phase in these samples are very close to those for the nonfluorinated T* phase regardless of the fluorination conditions. It is reasonable to consider this phase as the initial compound unaffected by $XeF_2$. The fluorinated phase exhibits a slightly decreased *c* parameter and a significantly increased *a* parameter in comparison with the initial *T** compound. A gradual increase of the amount of the fluorinated phase from $\approx$10% (sample 2) to $\approx$50% (sample 5) was observed during the increase of the temperature and time of fluorination. For 350°C (6) only the fluorinated T* compound was obtained. Weak, very broad reflections corresponding to LaOF were observed when the temperature of the fluorination was further increased to 400°C (7). The cell parameters and cell volume of the fluorinated T* phase, as measured from powder X-ray diffraction, are listed in Table 1.

Measurements of the temperature dependence of the magnetic susceptibility showed that none of the samples exhibited superconductivity down to 12 K.

**TABLE 1**
**Fluorination Conditions and Cell Parameters of the Fluorinated T* Phase**

| Number | Fluorination conditions | *a*, Å | *c*, Å | *V*, Å$^3$ |
|---|---|---|---|---|
| 1 | initial | 3.8368(4) | 12.533(2) | 184.50 |
| 2 | 200°C, 30 h, 1$XeF_2$ | 3.935(1) | 12.522(6) | 193.89 |
| 3 | 300°C, 15 h, 1$XeF_2$ | 3.8893(4) | 12.522(2) | 189.40 |
| 4 | 300°C, 30 h, 1$XeF_2$ | 3.884(1) | 12.521(4) | 188.88 |
| 5 | 300°C, 100 h, 1$XeF_2$ | 3.872(1) | 12.517(2) | 187.66 |
| 6 | 350°C, 200 h, 1.5$XeF_2$ | 3.8783(5) | 12.513(2) | 188.21 |
| 7 | 400°C, 100 h, 1$XeF_2$ | 3.858(1) | 12.507(4) | 186.16 |

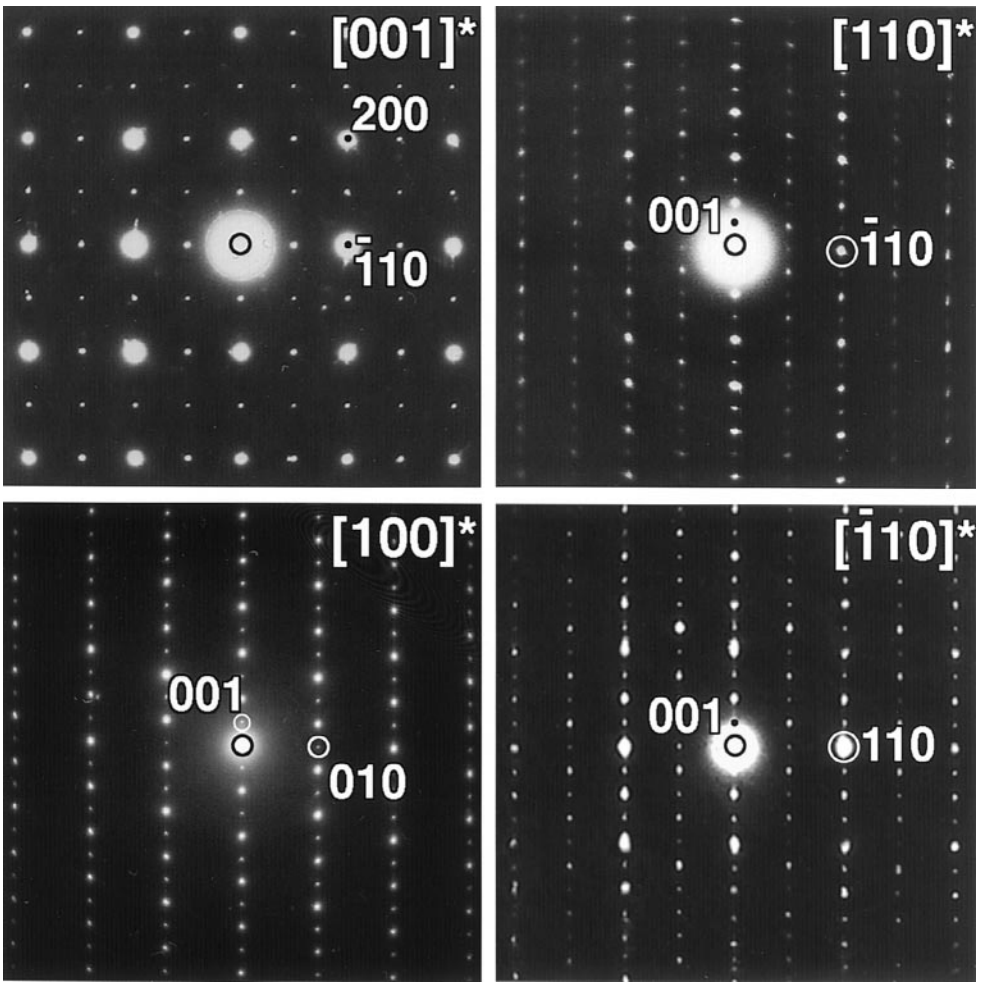


**FIG. 2.** [001]*, [100]*, [110]*, and [$\bar{1}$10]* electron diffraction patterns of the A phase.

The ED and HREM investigations revealed that all fluorinated samples have a complicated microstructure. The analysis of numerous ED patterns taken along different zone axes allows us to attribute them to two phases with a similar T* sublattice but showing different superstructures which will be abbreviated as *A* and *B*. These phases were observed in all samples regardless of the fluorination temperature.

Figure 2 reproduces the ED patterns of the [001]*, [100]*, [110]*, and [$\bar{1}$10]* zone axes (with the indexing referring to the tetragonal unit cell of the initial compound) of the A phase. Superstructure spots at the $(h + 1/2, k + 1/2, l)$ positions are visible in the [001]*, [110]*, and [$\bar{1}$10]* patterns, whereas in the [100]* pattern no additional reflections were observed. Measuring the angle between different vectors of the reciprocal cell revealed deviations from 90° between the [001]* and [110]*, [001]*, and [100]* directions, which indicate the monoclinic distortion. The [001]* and [110]* sections of reciprocal space show rectangular two-dimensional lattices. According to this, [$\bar{1}$10]* was chosen as the $b_m^*$ vector of the new monoclinic supercell. The whole set of diffraction patterns can be indexed using the cell parameters: $a_m = a\sqrt{2}$, $b_m = a\sqrt{2}$, $c_m = c$, and $\beta = 91.4°$, where *a*, *b*, and *c* are the basic vectors of the T* phase. Figure 3 shows an ED pattern with split reflections taken from a twinned region of the A phase. The 00*l* row is unsplit, which indicates that the (001) plane is the twin plane. The formation of twins confirms the monoclinic structure and allows an accurate measurement of the $\beta$-angle. It should be noted that no extinction conditions were found in the ED patterns of the A phase, as was checked by tilting experiments.

The [001]*, [100]*, and [110]* ED patterns of the B phase (Fig. 4) are very close to those for the tetragonal T* phase. The [001]* ED patterns of the B phase show a small difference between the repeat periods along the [110]* and [$\bar{1}$10]* directions which corresponds to the formation of an orthorhombic unit cell. The [110]* ED pattern of the

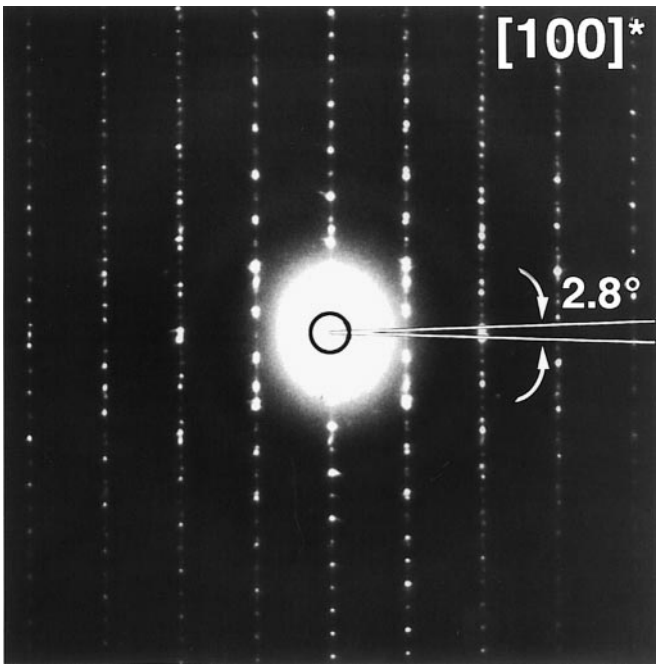


**FIG. 3.** [100]* pattern of a twinned area, confirming the monoclinic structure of the A phase.

B phase shows diffuse satellite spots with a modulation vector $q \approx 1/6\ [\bar{1}13]^*$. Only the first satellite of this modulation is visible, pointing toward a sinusoidal modulation. This incommensurate modulation is very similar to the modulation of the Bi-based or some of the Tl-based superconductors in the 2212 or the 2223 family (see, e.g., (11)). We will come back to this when discussing the corresponding HREM images.

Besides the single phase ED patterns, [110]* patterns were found which are produced by the overlapping of patterns of the A phase and the B phase (Fig. 5). The corresponding low magnification multibeam TEM image shows bright A and dark B bands alternating along the *c*-axis, separated by interfaces which are roughly parallel to (001). The A phase forms narrow (60–100 Å) strips placed in a matrix of the B phase.

A detailed examination of the ED pattern from Fig. 5 reveals a splitting of the reflections along $c^*$ which can be attributed to different subcell dimensions of the A phase and the B phase along the *c*-axis; an enlarged pattern is shown in Fig. 6, where the A and B reflections are indicated. The *hk*0 reflections are unsplit due to close subcell dimensions of both phases in the *a*–*b* plane. Assuming the value of $a = 3.88$ Å as determined from X-ray data, one can propose the subcell dimensions of $c = 12.84$ Å and $c = 12.53$ Å for the A and B phases, respectively. The subcell parameters of the B phase are very close to those determined from the X-ray data.

The [110] HREM image in Fig. 7 shows the boundary between both phases. The correspondence between the HREM images and the different types of superstructure

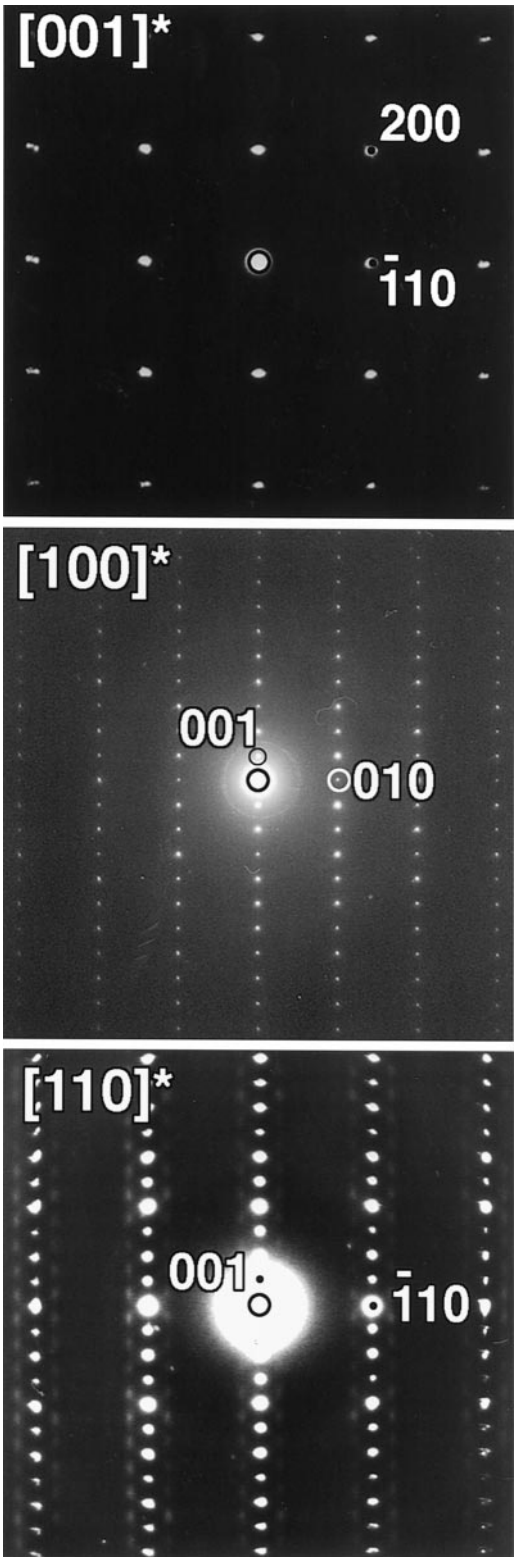


**FIG. 4.** [001]*, [100]*, and [110]* ED patterns of the B phase.

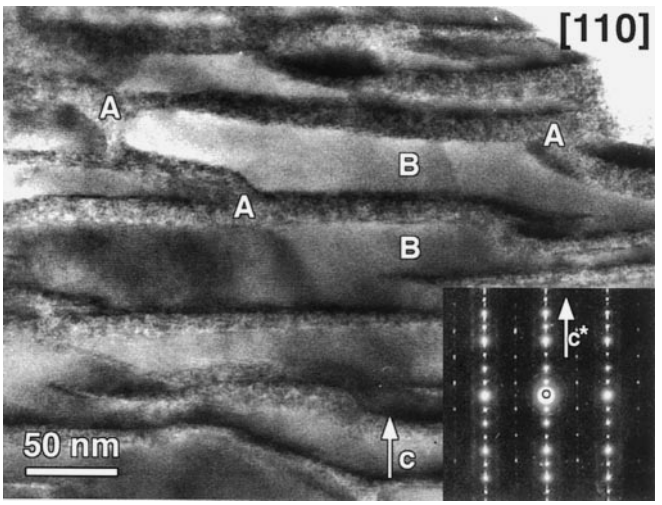


**FIG. 5.** Low magnification image along the [110] axis, showing the bands formed by alternating A and B phases. The corresponding ED pattern is shown in the inset.

observed on the ED patterns was established using a computer simulated Fourier transform, which is also shown in Fig. 7. The area belonging to the A phase clearly exhibits an alternation of bright and dark dots along [110] with a repeat period $\approx 5.5$ Å which is in agreement with the proposed unit cell for this phase. An interesting feature is the identical contrast corresponding to the $(La_{0.75}Sr_{0.25}O)_2$ rock salt and $(La_{0.25}Ho_{0.75}O)_2$ fluorite-type layers. The HREM image of the B phase is very close to that of the initial structure. The modulated structure can be seen as a weak intensity modulation along the [110] direction, most pronounced in the rows of bright dots, corresponding to lattice distortions in the rock salt layers. The dark and bright areas are not always regularly spaced, but on the average the repeat period is equal to that found in the ED pattern. The type of modulation contrast in HREM is also similar to the one observed in undoped $La_2CuO_4$ (7); in that case, however, the modulation was strictly commensurate.

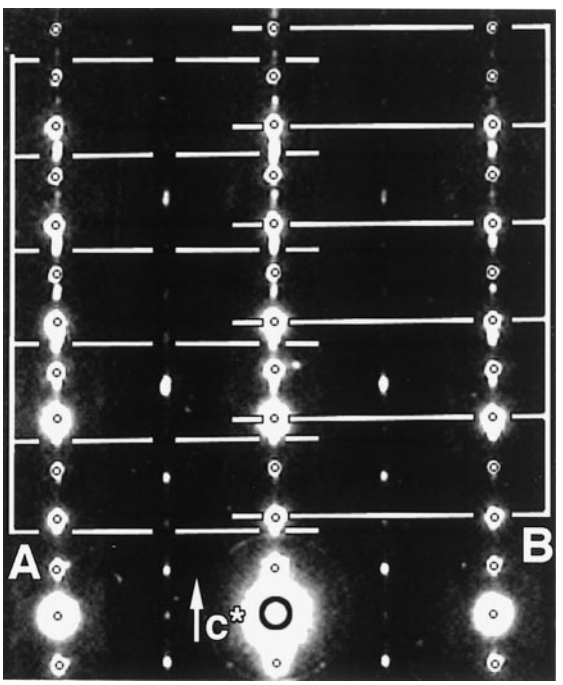


**FIG. 6.** Enlargement of an ED pattern from Fig. 5 clearly showing evidence for the different $c$ parameters of the A and B phase.

The small width of the bands of the A phase hampers accurate EDX measurements of the fluorine content in both phases. However, due to the existence of crystallites containing only the B phase, comparison can nevertheless be made. Numerous EDX measurements performed on B and A + B crystallites show the presence of fluorine in both structures. The spectrum obtained from A + B crystallites exhibits a much higher fluorine amount (Fig. 8a) in comparison with the crystallites containing only the B phase (Fig. 8b). This is clearly related to a higher concentration of fluorine in the A phase. However, due to the low $Z$-number of fluorine, no quantitative analysis can be made and the result is only an estimate. Both B and A + B crystallites have similar cation compositions which do not change in the range of standard deviations.

## DISCUSSION

TEM investigations of fluorinated T* samples reveal the presence of two closely interlinked fluorinated phases with dimensions close to the tetragonal subcell in the $a$–$b$ plane and with significantly different repeat periods along the $c$-axis. The values of the subcell parameters determined from the ED patterns for the B phase are very similar to those obtained from X-ray data. At the same time, the X-ray patterns do not exhibit any additional reflections which can be attributed to the presence of the A phase. This is related to the small width of the bands of the A phase along the $c$-axis which leads to significant broadening and decreasing intensity of the $hkl$ reflections of the A phase. The $hk0$ reflections should remain sharp but they are completely overlapped by reflections of the B phase due to the close $a$–$b$ dimensions.

The gradual change of the cell parameters of the B phase with the increase of the fluorination temperature (Table 1) allows us to relate it to the competition between the different reactions taking place during the interaction of the T* phase with $XeF_2$.

Previous investigations of the structural accommodation of extra anions in the T, T′, and T* compounds revealed that the $(CuO_2)$ planes are not strongly affected by anion insertion and that the structural changes take place mostly in the $(Ln_2O_2)$ fluorite or rock salt blocks. The extra anions in

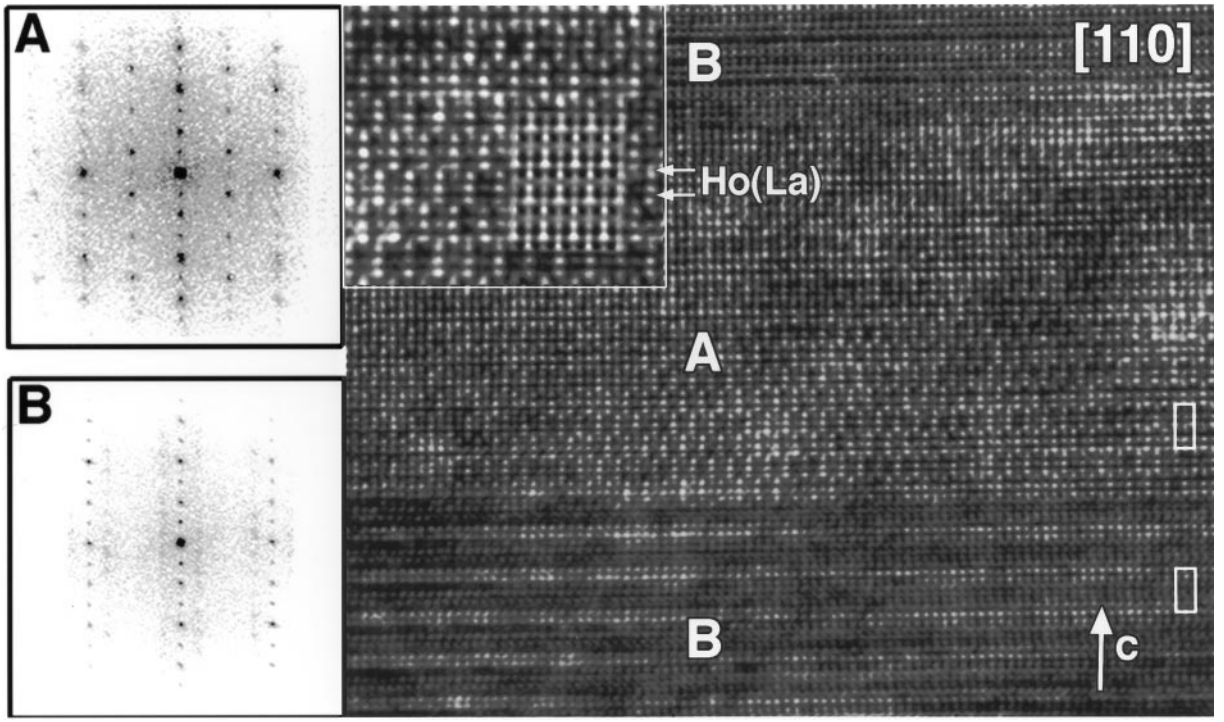


**FIG. 7.** HREM image of the interface between phases A and B with the optical diffraction patterns taken from regions of A and B phases. An enlargement of the A phase area, with the simulated image ($\Delta f = -40$ nm, $t = 2$ nm) of this structure included in the figure.

$La_2CuO_4$ (T-type structure) are accommodated at interstices located between the two rock salt LaO planes of the $La_2O_2$ slab (12, 13). These positions are coordinated by four $La^{3+}$ ions and four apical oxygen atoms. The fluorite-like structure of the $R_2O_2$ slabs with fully occupied anion positions, tetrahedrally coordinated by $R^{3+}$, and without apical oxygen is realized for $R_2CuO_4$ compounds with a T′ structure ($R$ = Pr–Gd) (8). Thus the interstitial positions in the T phase are the normal anion positions in the T′ phase. The particular feature of the T* structure is the presence of both fluorite and rock salt slabs alternating along the $c$-axis. Consequently, one may expect a competition between the fluorine insertion into the different structural blocks. Moreover there will be a redistribution of anions between the fluorite and rock salt blocks.

Our investigations of the fluorination of the T′ $Gd_2CuO_4$ phase did not reveal any noticeable interaction between this phase and $XeF_2$ at different temperatures up to the decomposition of the T′ phase at 500°C. One can therefore conclude that the fluorite slab is hardly subjected to fluorine insertion. The extra anions can be accommodated in the cavities of the rock salt slab of the T* phase. This reaction takes place at low fluorination temperature and leads to an enlargement of the $a$ parameter due to the repulsion between the apical oxygen atoms of the $CuO_5$ pyramids and the interstitial fluorine atoms. Indeed, this effect is clear when comparing the $a$ parameters for the initial T* phase and sample 2 (Table 1). A similar unit cell expansion was observed for fluorinated $La_2CuO_4$ where the fluorine insertion leads to the increase of the dimensions of the $K_2NiF_4$ subcell from 3.803 to 4.038 Å (7). At higher temperatures the anion exchange of oxygen by fluorine becomes the primary reaction. The oxygen released during this process is absorbed by the inner walls of the copper tube. The removal of apical oxygen atoms is accompanied by a contraction of the unit cell along the $c$-axis due to the formation of a square planar coordination of part of the Cu atoms. The decrease of the $c$ parameter from 12.533 to 12.507 Å for sample 7 provides indirect support for this assumption.

Ordering of anions and anion vacancies can be a reason for the appearance of different superstructures observed in the electron microscope. The intimate intergrowth of the A and B phases prevents the use of X-ray or neutron powder diffraction for the determination of the crystal structures of both phases, but it is possible to propose models of anion ordering and structural changes caused by the fluorination using the present ED and HREM observations.

The significant increase of the $c$ parameter for the A phase in comparison with the initial T* phase allows us to assume the appearance of additional apical anions for the Cu atoms. It should lead to the formation of an octahedral arrangement for part of the Cu atoms, followed by the increase of

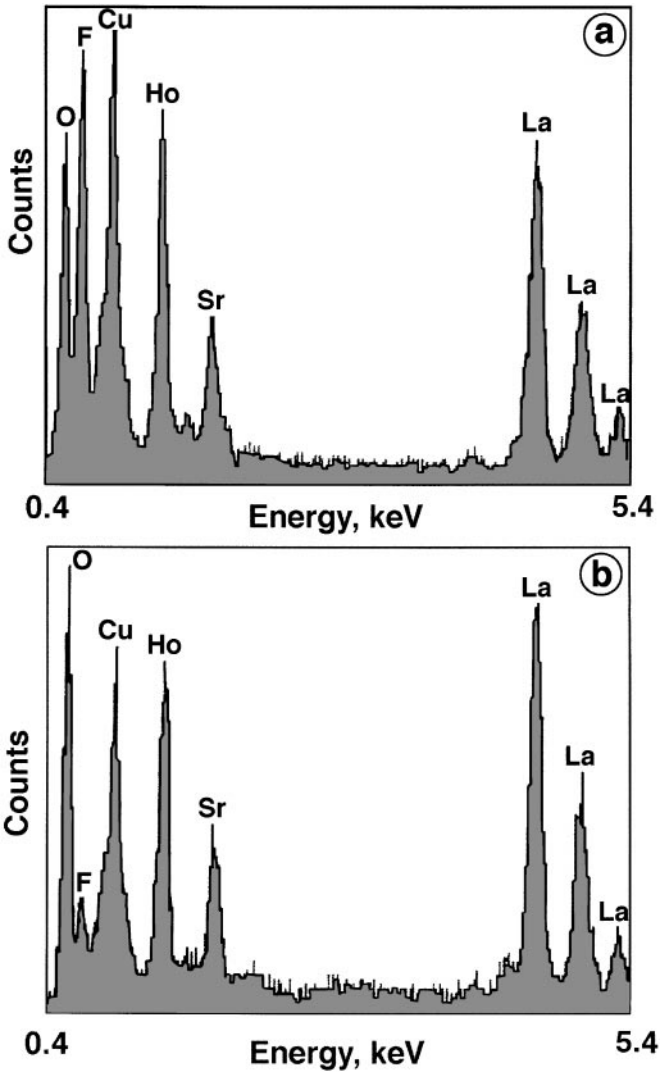


**FIG. 8.** EDX spectra of the A phase (a) and B phase (b).

the apical Cu–(O, F) distance, due to the Jahn–Teller effect, and by an enlargement of the $c$ parameter. The almost identical contrast produced by the initially different rock salt and fluorite slabs on the HREM image can arise from the redistribution of anions which results in a similar occupation of the anion positions in the $(La_{0.25}Ho_{0.75}O)_2$ and $(La_{0.75}Sr_{0.25}O)_2$ slabs. To determine the origin of the superstructure different variants of structural distortions were tested by comparison of calculated and experimental HREM images. The following possibilities were considered: the displacement of apical anions due to the repulsion from interstitial anions, the cooperative tilting of Cu–O polyhedra, the ordered placement of interstitial anions into $(A_2O_2)$ slabs and cation displacements in these slabs due to interaction with interstitial anions. The correspondence between the calculated and the experimental [110] HREM images was found to be satisfactory only when cation displacements in the $(A_2O_2)$ slabs were taken into account. A model of the structure of the A phase used for the image simulation is shown in Fig. 9a. The apical anion positions in both blocks were assumed to be statistically occupied and the variation of the occupancy factors does not produce significant changes in the calculated HREM images. Only one half of the interstitial positions in both blocks are occupied: these interstitial anions are ordered in a square manner in which there is an alternation between vacant and occupied interstitial positions in all {110} directions. The cooperative displacements of the cations in the $a$–$b$ plane are in "antiphase" in the neighboring $A$(O, F) and (O, F)$A$ layers: if the cations in the A(O, F) layer are displaced toward the interstitial anion, while the cations in the neighboring (O, F)A layer are displaced outward and vice versa. The position of the Cu cations was left unchanged (Fig. 9a).

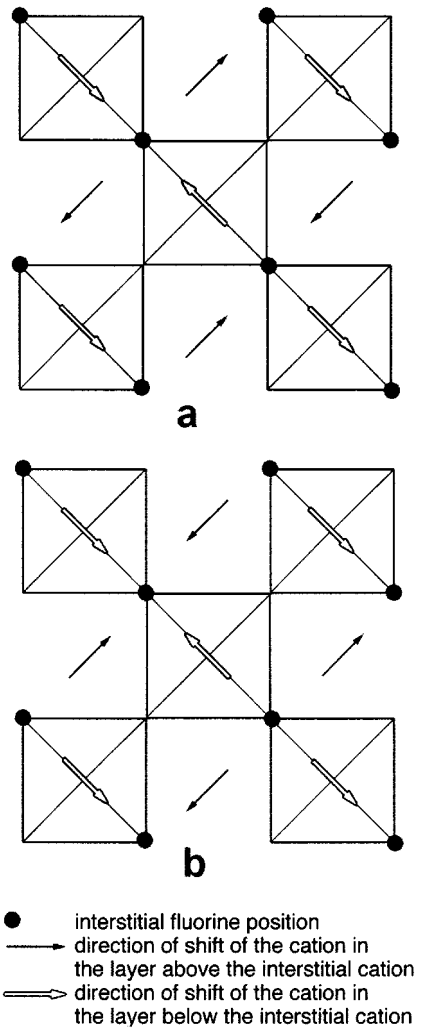


**FIG. 9.** Schematic representation of the cation displacements in the structure of the A phase used for the Madelung's constant computation: (a) anti-phase displacement; (b) in-phase displacement.

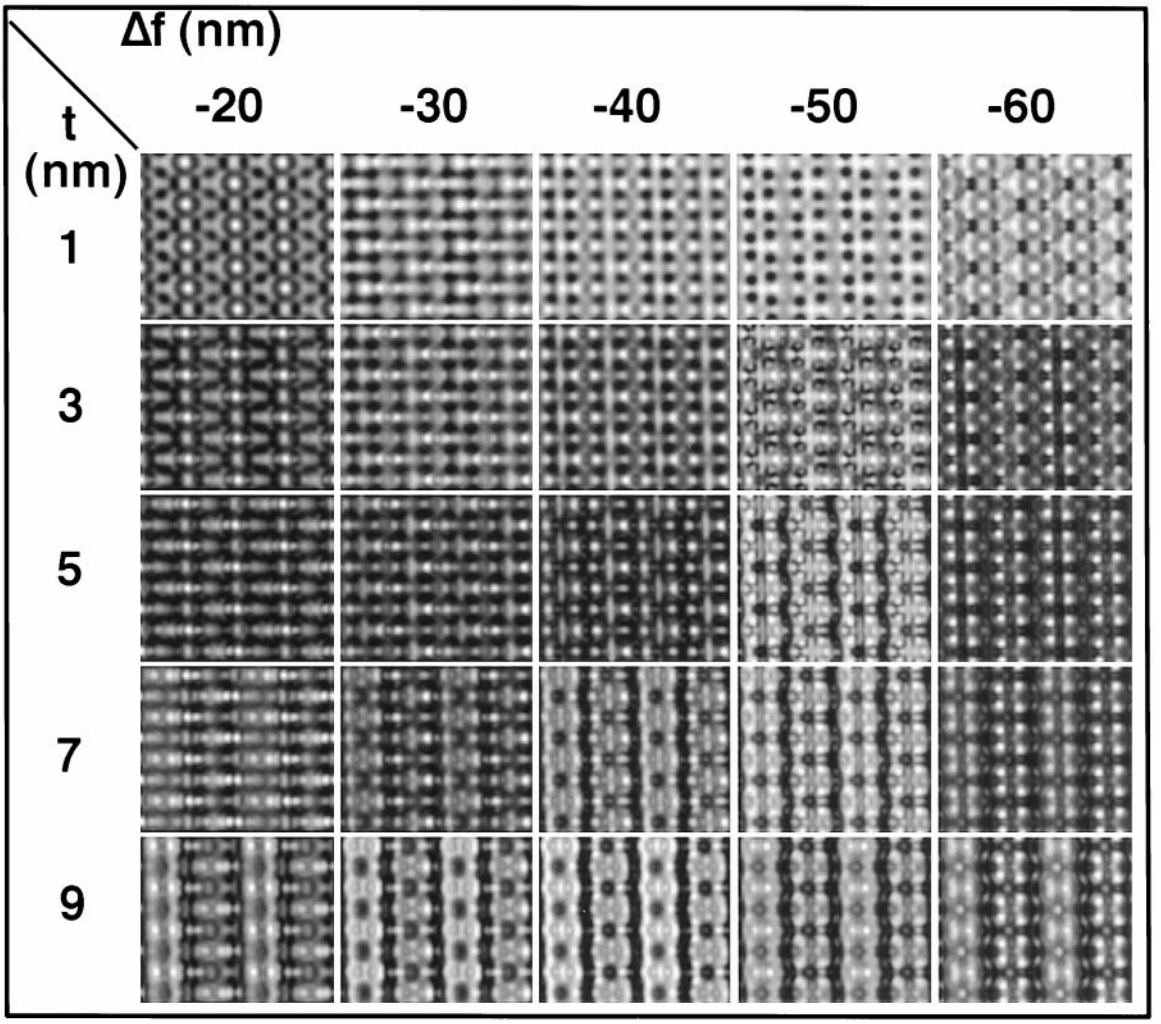


**FIG. 10.** Calculated [110] HREM images for the model of the A phase for different thicknesses and defocus.

Figure 10 shows the [110] HREM images for the described model, calculated for different thicknesses and defocus values, using the monoclinic spacegroup *Pm*. The calculated images (Fig. 10) are in a good agreement with the experimental image (Fig. 7). In the inset of Fig. 7 a simulated image is shown for a defocus value of $-40$ nm and a thickness of 2 nm.

To understand the reason of the cation displacement a semiquantitative measurement of electrostatic energy was performed by computing the Madelung's constant. It should be noted that an absolute value of the electrostatic energy is meaningless for HTSC compounds because of the strong covalent bonding in the ($CuO_2$)-planes. Nevertheless, it is possible to use the value of the change in Madelung's constant ($\Delta\alpha$) during the variation of the structure parameters in the rock salt and fluorite slabs since the interaction between rare-earth cations and oxygen or fluorine atoms can be considered as mostly ionic. The dependence of Madelung's constant on the relative cation displacement in the $a$–$b$ plane has been computed by Ewald's method of convergent series using an algorithm described in (14). The calculations were made on the basis of the structure model described above; the A cation positions from the initial T* structure were chosen as a starting point [10]. Two possibilities were compared:

(a) an "antiphase" cation displacement in neighboring $A$(O, F) and (O, F)$A$ layers;

(b) an "in phase" cation displacement where the $A$ cations in both $A$(O, F) and (O, F)$A$ layers are shifted toward the same interstitial positions (Fig. 9b).

The dependence of $\Delta\alpha$ on the value of the atomic displacements is plotted for both cases in Fig. 11. The "antiphase" displacement is accompanied by a decrease of Madelung's constant and, consequently, leads to a relative stabilization of the crystal structure. The structure with in phase cation displacement shows the opposite behavior. On the basis of

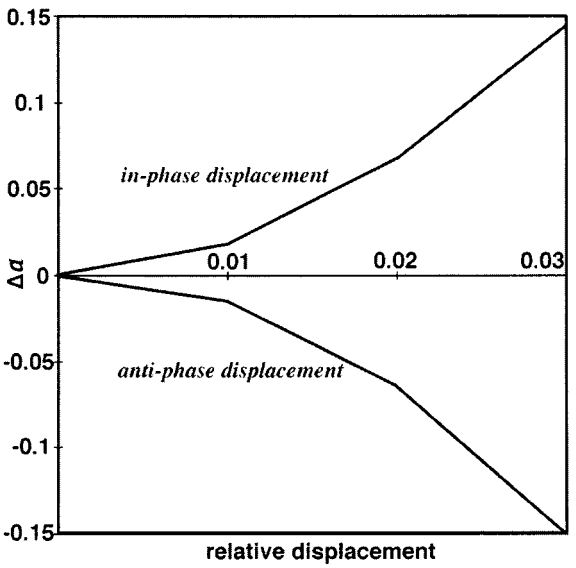


**FIG. 11.** Plot of the dependence of $\Delta\alpha$ on the value of the atomic displacement.

this consideration one may assume that the cation displacements within $(A_2O_2)$ layers are caused mostly by the electrostatic interaction with ordered interstitial anions.

For the *B* phase fluorine has been proposed to be only in the vacant interstitial positions of the $(La_{0.75}Sr_{0.25}O)_2$ slabs, an assumption supported by the HREM image (Fig. 12), where the modulations primarily appear in the rock salt layers. The diffuse character of the modulation hampers the comparison between experimental HREM images and images calculated using possible structure models. However, we can assume that the formation of this modulated structure is caused mainly by interaction between additional anions in tetrahedral interstices of rock salt blocks and apical oxygen atoms of $CuO_5$ pyramids. In this case the insertion of fluorine will lead to tilting of the $CuO_5$ pyramids to increase the distance between fluorine and the apical oxygen atoms. The apical oxygen atoms which are in between two fluorine anions are removed due to the reduction of the distance between these anions. In this way there will be an alternation of blocks with all interstitial positions fully occupied and without apical oxygen and blocks with normal T* structure (Fig. 13). The atomic coordinates were calculated according to the determined orthorhombic cell with the most symmetrical space group which agrees with the extinction conditions, *Ima*2. The calculated HREM image for a defocus of $-40$ nm and a thickness of 3 nm shows a reasonable agreement with the experimental one (the inset of Fig. 12).

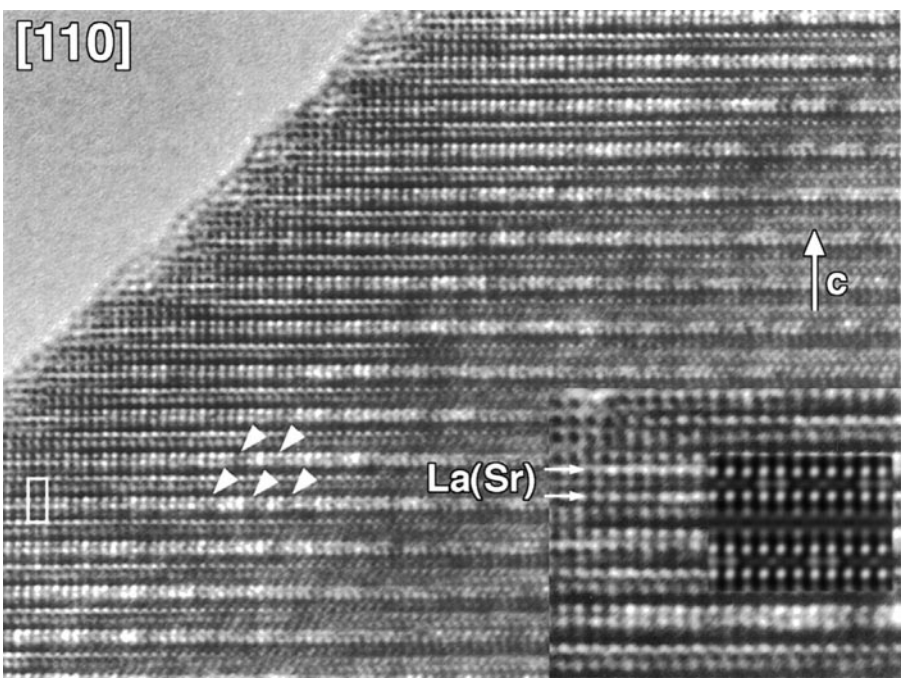


**FIG. 12.** The [110] HREM image of the B phase. The calculated HREM image for a defocus of 40 nm and a thickness of 3 nm is shown in the inset.

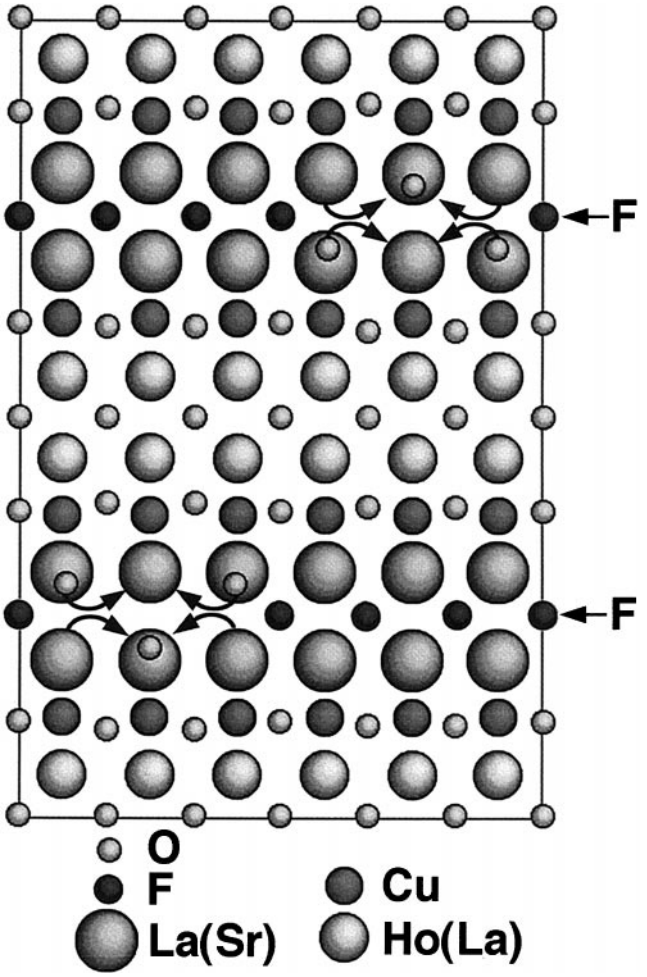


**FIG. 13.** Model of the structure of the B phase viewed along the [110] direction.

## CONCLUSIONS

The fluorination of the T* phase using $XeF_2$ produces samples with a complex microstructure due to the competing reactions of fluorine insertion, anion exchange, and anion redistribution between rock salt and fluorite blocks. The formation of two closely interlinked phases with different superstructures was observed. The A phase has a monoclinic unit cell with parameters $a_m = a\sqrt{2} \approx 5.5$ Å, $b_m = a\sqrt{2} \approx 5.5$ Å, $c_m = c = 12.84$ Å and $\beta = 91.4°$. A possible reason for the formation of this superstructure is the similar anion arrangement of the initially different $(La_{0.25}Ho_{0.75}O)_2$ and $(La_{0.75}Sr_{0.25}O)_2$ slabs. The anion redistribution is accompanied by ordering of vacant and occupied interstitial positions followed by a displacement of A cations due to electrostatic interaction with ordered anions. The A phase forms narrow bands within the matrix of the orthorhombic B phase. This B phase has fluorine in part of the interstitial positions between the $(La_{0.75}Sr_{0.25}O)_2$ slabs, with the removal of neighboring apical oxygen atoms. Blocks with occupied interstitial positions and absent apical oxygen atoms alternate in an ordered manner with blocks in which the rock salt part is preserved, thus creating an orthorhombic structure, which, however, is modulated due to a pseudo-periodic lattice distortion, mainly within the rock salt slabs.

## ACKNOWLEDGMENTS

This work has been performed in the framework of NATO Grant HTECH.LG 960325 and IUAP 4/10. It is partially supported by the Russian Scientific Council on Superconductivity (Poisk), INTAS-932483ext, and RFBR-INTAS (00639 I-96). The authors are grateful to P. Kazin for magnetic measurements. A. Abakumov and O. I. Lebedev are grateful to DWTC (Belgium) and FWO (Belgium), respectively, for financial support during their stay.

## REFERENCES

1. A. C. W. P. James, S. M. Zahurak, and D. W. Murphy, *Nature* (*London*) **338,** 240 (1989).
2. U. Asaf, I. Felner, and U. Yaron, *Physica C* **211,** 45 (1993).
3. A. Tighezza, J. L. Rehspringer, and M. Drillon, *Physica C* **198,** 209 (1992).
4. B. M. Tissue, K. M. Cirillo, J. C. Wright, M. Daeumling, and D. C. Larbalestier, *Solid State Commun.* **65,** 51 (1988).
5. B. Chevalier, A. Tressaud, B. Lepine, K. Amine, J. M. Dance, L. Lozano, E. Hickey, and J. Etourneau, *Physica C* **167,** 97 (1990).
6. M. H. Tuilier, B. Chevalier, A. Tressaud, C. Brisson, J. L. Soubeyroux, and J. Etourneau, *Physica C* **200,** 113 (1992).
7. A. M. Abakumov, J. Hadermann, G. Van Tendeloo, R. V. Shpanchenko, P. N. Oleinikov, and E. V. Antipov, *J. Solid State Chem.* **142,** 440 (1999).
8. F. Izumi, E. Takayama-Muromachi, A. Fujimori, T. Kamiyama, H. Asano, J. Akimitsu, and H. Sawa, *Physica C* **158,** 440 (1989).
9. P. Lightfoot, S. Pei, J. D. Jorgensen, X.-X. Tang, A. Manthiram, and J. B. Goodenough, *Physica C* **169,** 15 (1990).
10. E. M. Kopnin, R. V. Shpanchenko, E. V. Antipov, and L. M. Kovba, *Superconductivity*: *Phys. Chem. Technol.* (*Russ.*) **5,** 1874 (1992).
11. H. W. Zandbergen, W A. Groen, F. C. Mijlhoff, G. Van Tendeloo, and S. Amelinckx *Physica C* **156,** 325 (1988).
12. M. H. Tuilier, B. Chevalier, A. Tressaud, C. Brisson, J. L. Soubeyroux, and J. Etourneau, *Physica C* **200,** 113 (1992).
13. C. Chaillout, S. W. Cheong, Z. Fisk, M. S. Lehmann, M. Marezio, B. Morozin, and J. E. Schriber, *Physica C* **158,** 183 (1989).
14. S. G. Popov and V. A. Levitzkiy, *Zh. Phys. Khim.* (*Russ.*) **LV81** (1981).